Quantitative experimental characterization of solidpropellant surface temperature before ignition for future model validation

Robin Devillers, Boulal Stéphane, Dupays Joël, Rommeluere Sylvain, Henry Didier

DOI: 10.13009/EUCASS2022-4446

Quantitative experimental characterization of solid-propellant surface temperature before ignition for future model validation

DEVILLERS Robin William, BOULAL Stéphane**, DUPAYS Joël***, ROMMELUERE Sylvain**** and HENRY Didier******

**, **, ***DMPE, ONERA, Université Paris Saclay, Palaiseau F-91123, France*

**robin.devillers@onera.fr, **stephane.boulal@onera.fr, ***joel.dupays@onera.fr*

*****, *****DOTA , ONERA , Université Paris Saclay, F-91123 Palaiseau, France*

***** sylvain.rommeluere@onera.fr, ***** didier.henry@onera.fr*

Abstract

A general approach is presented in order to estimate the surface temperature and laser power density for solid-propellant ignition studies. It includes an error estimation based on random Monte Carlo draws. The method was demonstrated with a simple phenomenological ignition model adjusted to experimental data obtained with a research AP/HTPB composition. As a first step, only three error sources were considered here. The camera acquisition rate and synchronization are found to have a large impact on the estimated laser power density. A Gaussian laser beam profile was considered to illustrate biases for spatially integrated signals: the apparent ignition happens at the same time as the first local ignition spots, but with shallower temperature slopes. The approach is very promising for the purpose of reducing experimental error levels.

1. Introduction

Solid propellants are commonly used in a wide range of civil and military propulsion applications. Composite propellants combine oxidizing powder, usually AP (Ammonium Perchlorate) grains, within a polymer matrix such as HTPB (Hydroxyl-Terminated PolyButadiene). As such, they burn without external oxidizer source, for instance in low-oxygen atmospheres. One of the key advantages of solid-rocket motors (SRM) is their simplicity: once ignited, they will generate the pressure and specific impulse evolution induced by the grain shape without additional control. The design of the ignition subsystem is paramount in ensuring the reliability of the SRM. Solid-propellant ignition studies have been reported in the literature for a long time [1]-[4]. Many additional references can be found in a general review [5]. Most models aim at describing the increase of the temperature at the solid-propellant surface up to levels that correspond to the onset of the combustion reactions. For instance, recent studies focus on detailed composite microstructures in order to investigate ignition trends [6] or introduce new modelling approaches [7].

Every ignition model requires experimental ignition data so as to adjust the input parameters to be representative of the specific propellant compositions. The most common set of experimental data is built on the measurement of the ignition delay as a function of the heating flux [8]-[9]. The dependency usually follows a power law with an exponent between -2.0 and -1.8 [6]. However, this empirical power-law description does not give access to a detailed phenomenological description. Also, it is not detailed enough to enable critical discussions on physical parameters such as the value of the surface temperature at the moment of ignitions or activation energy values. The transient determination of the surface temperature of a solid-propellant sample under a controlled heat flux from the ambient temperature up to the ignition temperature would give access to the complete ignition process and constitute a richer dataset.

At ONERA, ignition studies are conducted using an experimental set-up, which allows for the measurement of the surface temperature throughout the ignition process for initial nitrogen pressure up to 2.5 MPa. As for many past ignition studies [9]-[14], the ignition heat flux is induced by a laser source. Laser beams are easily triggered with controlled pulse durations and adjustable power values. Laser heat fluxes are also easier to estimate than heat flux from black powder set-ups or hot wire systems. The surface temperature is measured by IR devices including IR cameras

DOI: 10.13009/EUCASS2022-4446

calibrated in temperature [15]. This enables the conversion of the digital or electric signals to surface temperature quantities ranging from 290 to 700 K.
The quantitative determination of the surface temperature over time in absolute values, i.e. in [K] should be very helpful in the development and adjustment of ignition models. However, error levels associated with such measurements remain the key aspect to assess so that experimental data can truly assist modelling investigations. The aim of the present study is to provide a first estimation of the errors involved in the surface temperature estimation during ignition experiments. Experimental error levels are estimated by modelling surface temperature before ignition with a simple phenomenological model. A Monte Carlo approach is introduced in order to estimate dispersions induced by several non-correlated error sources. Specifically, three error sources associated to the measured systems are considered as well as the impact of the laser-beam non-uniformity. The proposed approach is demonstrated on two ignition measurements performed with a research solid-propellant composition.

2. Material and method

2.1. Surface temperature model

2.1.1.Ignition phenomenology

Before the ignition, i.e., the onset of the combustion reactions, the solid-propellant sample first heats up like a mere inert material [2][6]. The surface temperature variations $T_s(t)$ can be modelled as that of a semi-infinite 1D medium under a constant heat flux. Under additional assumptions (solid propellant with homogeneous properties, temperature-independent thermal properties), $T_s(t)$ is given by the following equation::

$$\boldsymbol{T_s(t) - T_s(0) = \frac{2}{b\sqrt{\pi}} \Phi_{laser} \sqrt{t}} \quad \textbf{(1)}$$

where $T_s(0)$ [K] is the initial surface temperature before heating, b [W K^{-1} m^{-2} s$^{1/2}$] is the propellant thermal effusivity, Φ_{laser} is the incident laser flux [W/m²]. Hence, the surface temperature $T_s(t)$ follows a square root function of time t.
Above a certain temperature, pyrolysis phenomena start in the solid propellant and induce a steeper temperature increase than inert heating [6][7]. The limit value at which pyrolysis starts is called the pyrolysis temperature T_{pyr} and usually sits between approx. 500 and 600 K depending on the composition and pressure. When the surface temperature reaches the ignition temperature T_{ign}, combustion reactions are triggered and hot gases starts getting ejected from the surface. T_{ign} is estimated between 600 to 700 K. Finally, the now-burning surface stabilizes at a temperature T_{burn}, which is usually found between 800 and 1000 K for usual composite propellants.

2.1.2.Simple demonstration model

The present uncertainty analysis does not aim at developing detailed and complete ignition models but only at estimate error levels for representative T_s trends during heating and ignition. As such, a simple demonstration model is used, which is based on the following assumptions and considerations:

- Inert heating phase following Eq. (1) with complete laser absorption on the surface ;
- Pyrolysis phase for temperature larger than T_{pyr}, with the additional temperature increment modeled by an arbitrary power law ;
- Instantaneous ignition when T_s reaches T_{ign}, i.e., T_s discontinuously jumps from T_{ign} to T_{burn}

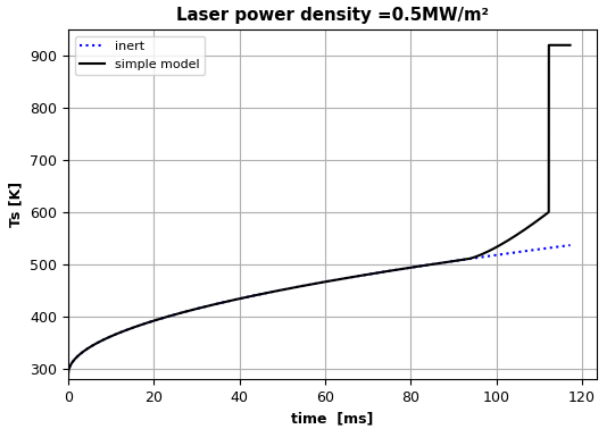

Figure 1. Example of simulated surface temperature computed by the simple demonstration model.
Blue dots: inert heating. Black line: complete model.

DOI: 10.13009/EUCASS2022-4446

The two threshold temperatures T_{pyr} and T_{ign} were adjusted manually to be consistent with the actual experimental data. T_{burn} was set to 920 K; it is only used to provide a rough luminance estimate of the burning surface, assuming an emissivity value of 1.0. As an illustrative example, a simulated $T_s(t)$ plot, computed for a laser power density of 0.5 MW/m², is shown on Figure 1

2.2. Experimental conditions: Solid-propellant parameters and combustion conditions

A classical composite solid-propellant composition used for research activities [15] was experimentally tested. It combines AP grains in an HTPB binder, both in typical proportions. Its effusivity b was measured around 800 $W.K^{-1}.m^{-2}.s^{1/2}$. This was used to compute the surface temperature evolution $T_s(t)$ during the inert heating phase according to Eq. (1). The samples are placed in a closed combustion chamber initially filled up with pure nitrogen of 0.3 MPa.. The reported experiments were obtained with samples with rectangular sections of approximately 6 x 5 mm². This was chosen in order to allow for relatively reduced useful frame dimension and consequently larger acquisition rates. In the following, two cases are presented corresponding to two laser power levels.

2.3. IR measurement devices

Three different IR measurement techniques were used for the ignition measurements. Table 1 provides their characteristics.

Table 1. IR measurement devices.

	Acquisition frequency f	Integration time
Camera FLIR	328 – 870 Hz	300 µs
Camera NOXANT	328 – 1700 Hz	25 µs
Radiometer	1000 - 5000 Hz	

2.3.1.IR Cameras

Two IR cameras were simultaneously used to cover a large temperature range. A FLIR Titanium camera (2007) was used to record temperature levels close to that of the ambient and its integration time was consequently set to the relatively large value of 300 µs. Recordings were performed with a maximum acquisition rate of 870 Hz (1/4 frame size). A NOXANT camera (2019) with higher performances was used to record temperature close to the sample ignition with a relatively short integration time of 25 µs. Recordings were possible up to an acquisition rate of 1700 Hz with appropriate windowing

2.3.2.IR radiometer

The radiometer consists of a Teledyne Judson InSb (Indium Antimonide) photodiode that collects light from the surface of the solid-propellant sample. The photodiode is mounted in a dewar and requires to be cooled down to a temperature of 77 K. This is done by liquid nitrogen. The dewar has been modified to receive a bandpass filter (3.4-4.0 µm) that cools itself down alongside with the detector. This considerably reduces the background noise. Thus, the radiometer allows for the measurement of surface temperatures lower than 100°C. The field of view is defined by an optical head composed of an IR lens and an IR optical fiber, which collects the light over a 3-mm-diameter disk appropriately contained within the sample surface. At the output of the fiber, another lens focuses the flux to the photodiode. The optical fiber allows to move the dewar at a reasonable distance of the combustion chamber. The radiometer is currently used at sampling frequencies ranging from 1 to 5 kHz depending on the experimental conditions. Prior to an ignition test, a hot solid surface (in practice, that of the tip of a soldering iron), placed at the location of the sample center, is aimed at by the radiometer. The orientation of the radiometer providing the higher signal level is then sought. Once found, its position is mechanically locked.

2.3.3.Temperature calibration

The temperature calibration curves are shown in Figure 2. The plots confirm the targeted temperature ranges of the two operated cameras, i.e., below 420 K for the FLIR camera and up to 620 K for the NOXANT camera. It also shows that the radiometer only gives access to temperature above 400 K. The calibration data were used to convert measured signals to temperature quantities and to generate realistic simulated measurements for the uncertainty analysis.

DOI: 10.13009/EUCASS2022-4446

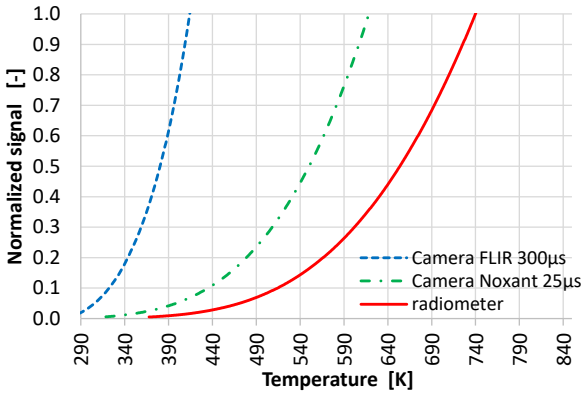

Figure 2. Temperature calibration plots for the employed measurement devices.

2.3.1.Laser beam characteristics

The ignition is achieved with the irradiation of the sample surface by a high-power CO_2 laser beam providing power density ranging from 0.1 to 2.0 MW/m². The laser-pulse duration was set between 40 to 500 µs. The laser beam profile of CO2 lasers follows a typical Gaussian profile [14], whereby the laser spatial irradiance $I_{laser}(r)$ is given by equation (2):

$$\boldsymbol{I_{laser}(r,z) = I_0 exp\left[-\left(\frac{r}{w(z)}\right)\right]} \quad \textbf{(2)}$$

where *r* stands for the radial position in the beam cross-section, *z* corresponds to the position along the beam path, *w(z)* is the laser-beam radius at position z and I_0 is the peak laser power density [W/m²]. In the model, the laser energy density was set between 0.3 to 4.0 MW/m². The laser spatial inhomogeneity was only considered for the measurements obtained with the radiometer, for which local ignition points cannot be determined and laser-beam spatial inhomogeneity matters. The beam radius *w(z)* was set to 7 mm in order to correspond to the laser beam dimension in the combustion chamber. A simulated laser-beam power density distribution, associated with a peak power of $I_0 =$ 1.0 MW/m², is shown in Figure 3.

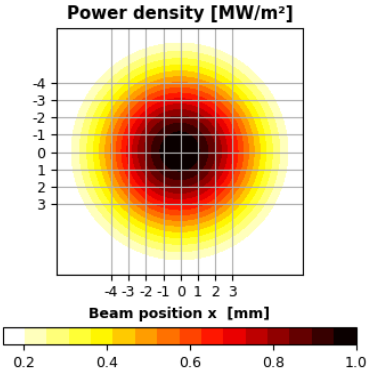

Figure 3. Laser-beam power density distribution for a peak power of $I_0 = 1.0$ MW/m².

2.4. Uncertainty analysis

2.4.1.General approach

The uncertainty analysis was performed by simulating realistic measurement signals and processing them like real data. For a given laser power density level, it follows the following steps:

a. Simulation of an ideal surface temperature $T_s(t)$ using the simple demonstration model of section 2.1.2;
b. Determination of an ideal digital measurement *DL(t)* by converting $T_s(t)$ using temperature calibration data (see Figure 3);

DOI: 10.13009/EUCASS2022-4446

c. Add various errors sources to obtain $DL_{error}(t)$;
d. Process $DL_{error}(t)$ as if it was real measurement data.

The aspects of the process are further detailed below.

2.4.2.Monte Carlo approach and considered error sources

A Monte Carlo approach is used in order to generate distributions for the studied parameters of interest. It is based on random draws for each of the tested uncertainty sources, following distributions representative of the considered error source [16][17]. The number of draws was fixed to $2x10^5$ with convergence checked for the targeted information, i.e. the standard deviation of the parameters of interest. Three uncertainty sources were considered in the present error analysis. They are listed in Table 2.

The first two sources are associated with the measurement devices themselves. Shot noise is a usual error source of every electrical system. It was modeled with a simple Normal distribution. The noise standard deviation σ was estimated to be below 1% of the measured signal, based on black body measurements at various temperatures. A single value of σ = 1% is considered as it represents a realistic noise value. The calibration uncertainty was estimated by comparing the interpolated calibration plot to the measured data at various black body temperatures. The resulting discrepancy was found between 1% and 2% in most of the temperature range with a couple of experimental dots leading to a 3% discrepancy. A normal distribution with σ = 3% was thus chosen to avoid underestimating calibration errors. The law for calibration error will be refined in future works.

The third error source relates to the uncertainty on the exact starting time of the laser pulse. A relatively small uncertainty has recently been found on the synchronization of the laser triggering. This manifests as a dispersion of the pulse starting time, i.e., of the time origin t = 0 s (see Eq. (1)). This error can be partially reduced by defining t = 0 s as the time at which an increase of T_s is first observed. However, the recordings are only obtained for discrete moments due to the finite acquisition frequency f. There remains an uncertainty on the pulse starting time corresponding to the time interval $dt = 1/f$. The error distribution was hence modeled with a uniform law of width $dt = 1/f$.

Table 2. Uncertainty sources. The symbols μ and σ stand for average value and standard deviation.

	Distribution type	**Parameter**	**Type**
Shot noise	Normal	μ=0; σ =1%	Measurement device
Temperature calibration	Normal	μ=0; σ =3%	
Laser starting time	Uniform	$dt = 1/f$	Laser synchronization

2.4.3.Influence of the laser-beam inhomogeneity

The non-uniformity of the laser-beam power density leads to an inhomogeneous heating of solid-propellant samples. Local spots follow different $T_s(t)$ evolutions depending on their locations within the beam profile, i.e., a steeper temperature increase is expected close to the Gaussian peak whereas a smoother one is expected close to the edges. The resulting signal results from the integration of various local temperature variations, which might happen with very different time scales in the case of an inhomogeneous beam.. The error associated to the laser-beam inhomogeneity was not investigated with random draws. However, its potential impact is illustrated by comparing three types of spatial-integration conditions, as described in Table 3. One integration condition considers the full sample surface (a rectangle 6 x 5 mm² surface area). The other two conditions correspond to the 3–mm diameter collection disk of the radiometer: one with the beam perfectly centered on the disk, the other one with the beam laterally shifted relative to the disk center.

Table 3. Spatial-integration conditions for the investigation of laser-beam inhomogeneity impact.

	Shape	**Dimensions**	**Laser-beam position**
Sample average	Rectangle	6 x 5 mm²	centered
Radiometer field-of-view	Disk	Diameter: 3 mm	centered
	Disk	Diameter: 3 mm	1.5 mm lateral shift

DOI: 10.13009/EUCASS2022-4446

2.4.4. Studied parameter: Laser power density estimation from temperature data

As shown in Eq. (1), the variation of $T_s(t)$ with $t^{0.5}$ follows a straight line with a slope proportional to the absorbed laser power Φ_{laser}. As such, the inert-heating phase is usefull in estimating the local absorbed power induced by the laser surface heating. This approach was applied on the simulated measurements, which generated a power density value for each Monte Carlo draw. A power density distribution is estimated from all the draws. The resulting standard deviation for the distribution $\sigma_{\Phi laser}$ was used to compare error levels for various experimental conditions (in the case of Gaussian distributions, error would be reported as ±2 $\sigma_{\Phi laser}$). As will be detailed later, $\sigma_{\Phi laser}$ was estimated below 17% for Φ_{laser} lower than 4.0 MW/m² for the tested experimental conditions, i.e. an error below ±34% on the laser power density.

3. Results

This section starts with the analysis of the experimental data obtained from the two ignition cases performed on the research-type solid-propellant composition (section 3.1). The data were then used to adjust the simple ignition model (section 3.2). Uncertainty analysis is detailed for homogeneous laser heating (section 3.3) and Gaussian beam profile with the radiometer (section 3.4).

3.1. Experimental ignition data

Two ignition tests were performed for two laser-power settings, labeled “low-level” and “high-level”. Images recorded by the NOXANT camera are shown in Figure 4. Both tests show ignition from local spots, which heat up faster. For each test, the local surface temperature of the spots that ignited first is analyzed. This significantly eases the interpretation since, for these spots, the only heat flux leading the surface from rest conditions to ignition is that coming from the laser, whereas for the neighboring spots, the heat flux also contains that emitted back to the surface by the early flame radiation.

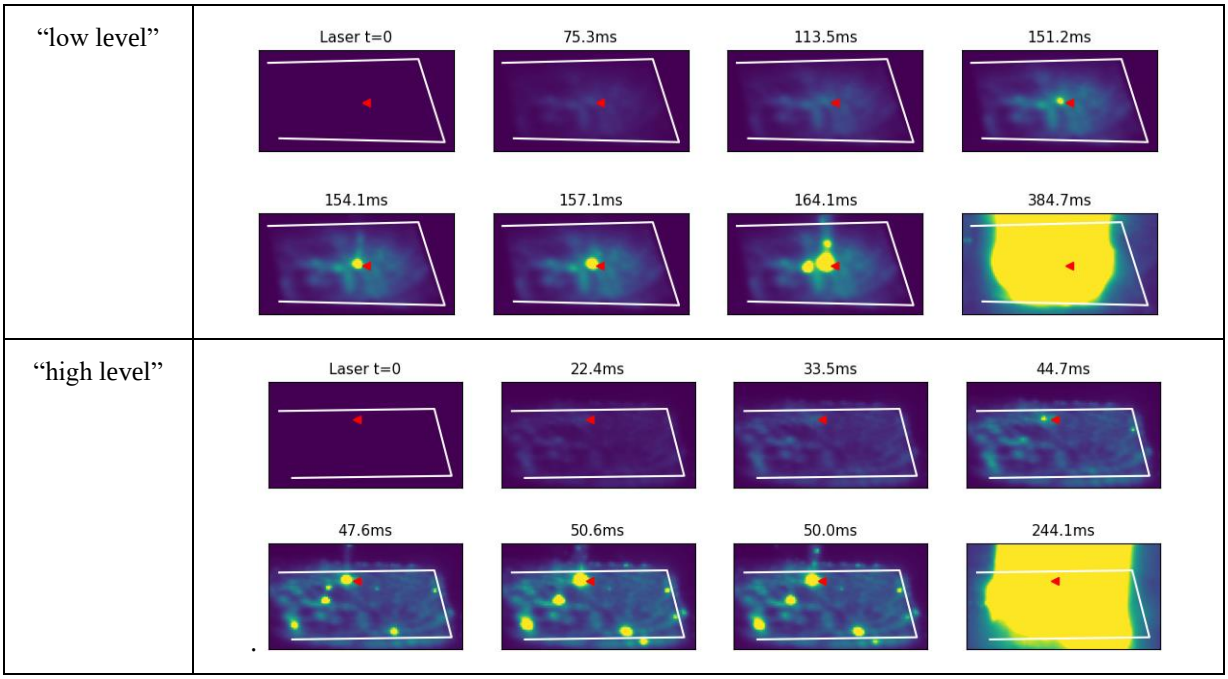

Figure 4. IR images recorded by the NOXANT camera for the “low-level” and “high-level” ignition tests. The first ignition spot is shown with a red triangle. White lines: sample borders.

For the “low level” test, the surface temperature of the first ignition spot is plotted in Figure 5 a). Note that no emissivity correction was applied, i.e., the surface emissivity is considered to be 1.0. The temperature evolution in Figure 5 a) shows a general shape that is consistent with the simple model proposed in 3.1.1, i.e., with an initial curvature and a temperature jump when the ignition occurs. The variation of $T_s(t)$ as a function of $t^{0.5}$ is linear until 450 K. These observations validate the modeling assumption considered, i.e., that the heating of the sample surface can be treated as that of that of a semi-infinite 1D medium. The laser power density Φ_{las} was estimated for the two ignition tests by

DOI: 10.13009/EUCASS2022-4446

estimating the slope of $T_s(t)$ vs $t^{0.5}$. The "low-level" test returned a value $\Phi_{las} \approx 0.42$ MW/m² whereas the "high-level" returned$\Phi_{las} \approx 0.82$ MW/m².
The signal measured by the radiometer for the "low level" test is shown in Figure 6 a). It appears rather noisy with a strong change in slope between 150 ms and 160 ms, which also correspond to that deduced from the IR camera recording (see figures 4 and 5 a)). The radiometer integration disk integrates signal over a 3 mm-diameter portion of the solid-propellant sample, i.e. with different local temperature variations, but the steepest slope change happens as the same time as forthe first ignition spot. After conversion to a temperature quantity, the plot of Figure 6b) shows only a small increase in temperature before ignition: the slope steep change happens for an apparent temperature of 370 K only. The luminance acquired by the radiometer is collected over a large measurement area, leading to a strong averaging effect that reduces the apparent temperature. In comparison with the evolution of T_s recorded by the IR camera (see Figure 4 a)), that recorded by the radiometer displays an apparent inconsistency. The slope determination method was also employed on the data measured by the radiometer (Figure 6). As expected, the estimated laser power density, $\Phi_{las} \approx 0.26$ MW/m², is approximately half of that obtained by the IR camera.

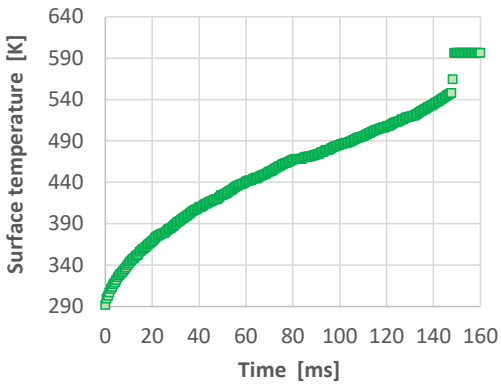

a) $T_s(t)$ vs t

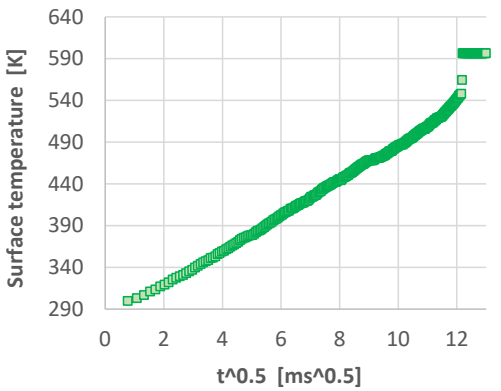

b) $T_s(t)$ vs $t^{0.5}$

Figure 5. Surface temperature of the first ignition spot for the "low-level" ignition test. Data obtained by the NOXANT camera.

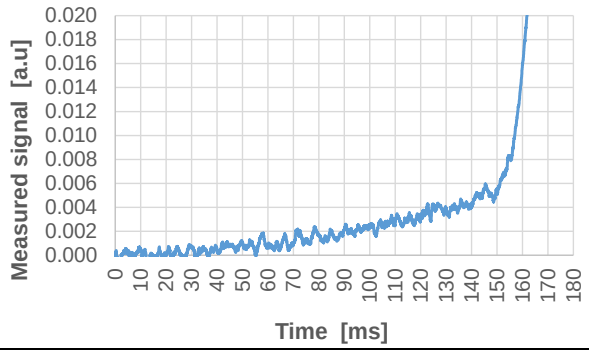

a) Measured signal

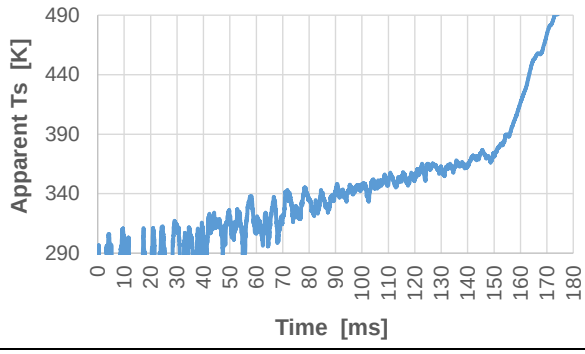

b) Measured temperature over the field-of-view

Figure 6. Radiometer measurements for the "low level" ignition test.

3.2. Simulated ignition conditions

3.2.1.Model-parameter adjustments

The simple model was adjusted to provide surface temperature evolutions consistent with the experimental data (IR camera) for the two power density levels (Figure 7). In each case, the experimental data corresponds to the surface temperature of the 1st ignition spot. The temperature T_{pyr} was set around 520 K and T_{ign} around 600 K. Both values seem a bit low. This is partly due to the absence of surface emissivity correction assuming an emissivity of 1.0 leads to underestimation of the measured temperature. Still the crude model is fairly consistent with the experimental data, even if it slightly overestimates the ignition delay for the low level test (10% overestimation). The discrepancy is low enough to enable a representative uncertainty analysis.

DOI: 10.13009/EUCASS2022-4446

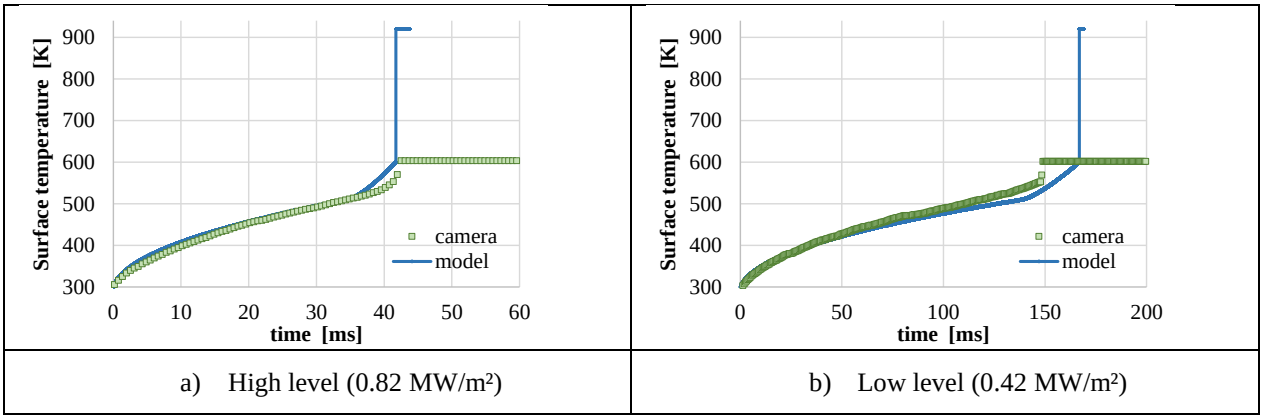

Figure 7. Surface temperature evolution for the two ignition tests with the adjusted simple model.

3.2.1.Simulated conditions

Surface temperature was simulated with the simple model for laser power density ranging from 0.3 to 4.0 MW/m² leading to ignition time ranging from 312 ms down to less than 2 ms. Figure 8 shows the evolutions of the surface temperature for various power levels. The corresponding variation of the the ignition time as a function of the power density plot is shown on Figure 9. It is consistent with experimental trends observed in the literature [6].

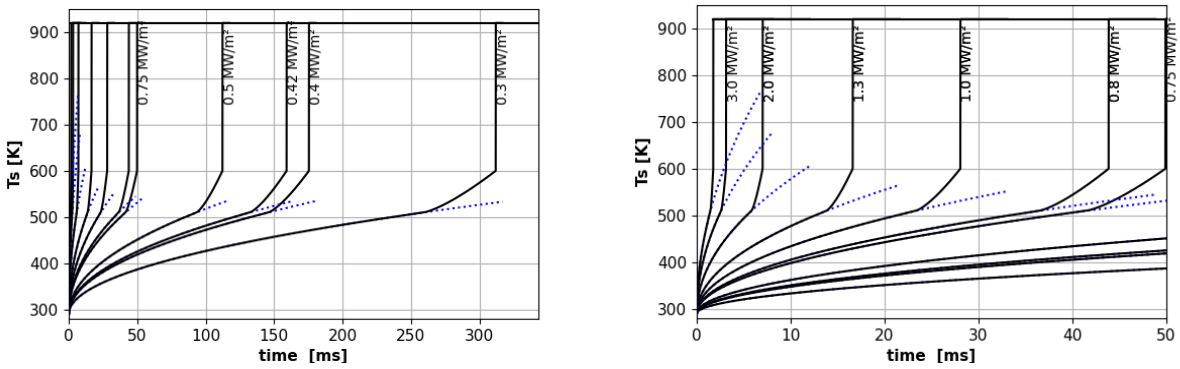

Figure 8. Simulated surface temperature evolutions determined by the simple model for laser power density ranging from 0.3 to 4.0 MW/m².

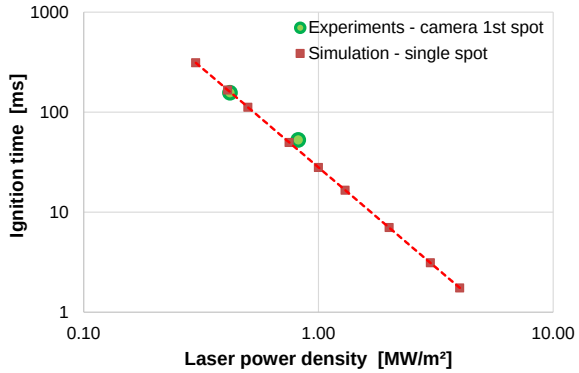

Figure 9. Ignition time as a function of the laser power density for measured and simulated data.

DOI: 10.13009/EUCASS2022-4446

3.3. Uncertainty for homogeneous or local laser heating

Uncertainty is first presented for homogeneous laser heating, e.g. for an ideal homogeneous beam profile or for single spots on a propellant sample. Here, the focus is placed on the error associated with the estimation of the laser power density from temperature evolutions $T_s(t)$ alone. This error corresponds to the dispersion on the laser power density values for all the Monte Carlo draws, estimated via the power density standard deviation. Figure 10 shows excellent convergence of the estimated standard deviation as the number of draws increases (up to $2x10^5$). Two conditions are shown in Figure 10. For the FLIR camera at an acquisition rate of 328 Hz and a mean laser power density of 1.0 MW/m² (a)), the measured standard deviation is 0.15 MW/m², i.e. 15% of the mean value For the NOXANT camera at an acquisition rate of 1700 Hz and a mean laser power density of 0.5 MW/m² (b)), the standard deviation is found to be below 0.003 MW/m², i.e. below 0.6% of the mean value . Even if the error levels are very different between the two cases, the convergence is similar with no significant variation in the standard deviation value above $5x10^4$ draws. A larger number of draws would certainly be necessary if additional error sources were considered or if each error source had a larger standard deviation itself.

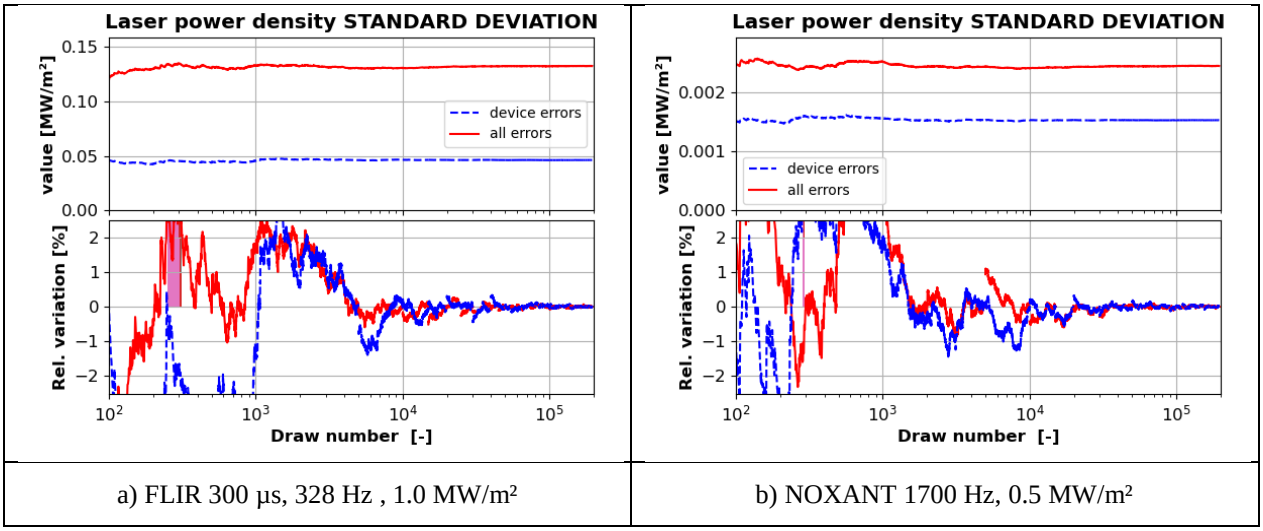

a) FLIR 300 µs, 328 Hz , 1.0 MW/m²

b) NOXANT 1700 Hz, 0.5 MW/m²

Figure 10. Monte Carlo convergence for the standard deviation of the estimated laser power density.

Examples of draws are shown in Figure 11 corresponding to the two camera types and to the two laser power density levels of 0.5 and 1.0 MW/m². For each case, the surface temperature evolution $T_s(t)$ is plotted for the full simulated case as well as for two cases of error assumptions: in blue squares, the two measurement device errors only, in red circles, all three error sources. Again, the variations of $T_s(t)$ are plotted as functions of t and of $t^{0.5}$ in order to illustrate the impact of draws on the estimated laser power density (based on the slope of $T_s(t)$ vs $t^{0.5}$). The limited integration time of the FLIR camera only allows for temperature measurements below 420 K, leading to a reduced number of measurement points for the larger power density levels. For instance, only three images are acquired before saturation for the case of a laser power density of 1.0 MW/m². This explains the much larger standard deviation on the estimated laser power density.

Laser-power density histograms are plotted on Figure 12 for the two cameras. Two acquisition rates are shown for the NOXANT camera in order to illustrate the effect of frequency and temperature range. It confirms that the histograms for the device error sources (blue histograms) are much narrower than for all three error sources (red histograms), suggesting that the uncertainty on the laser starting time is the most detrimental error source. The plots also show that the error significantly increases with increasing laser power density because of the much shorter ignition times. Finally, for a given laser power density (for instance 1.0 MW/m²) an increase of the acquisition rates significantly reduces the error as shown with the histograms for the NOXANT camera at acquisition rates of 328 and 1700 Hz.

Figure 13 shows the standard deviation on the laser power density as a function of the targeted laser power density (i.e. the value used to simulate $T_s(t)$) for the two cameras. The standard deviation is normalized by the power-density value used in the simulation. Various acquisition rates are shown for each camera. The thick line plots consider all three error sources whereas the dashed-line plots only include the two camera error sources. As shown with the previous histograms from Figure 12, the uncertainty is much lower when only the device error sources are considered. A reduction of the uncertainty on the laser initial time will have a significant impact on the overall uncertainty. Moreover, an increase of the acquisition rate significantly improves the measurement precision. At 1.3 MW.m², the standard

DOI: 10.13009/EUCASS2022-4446

deviation of the NOXANT camera reduced from 10% to 2.5% when the acquisition rate increased from 328 Hz to 1700 Hz.

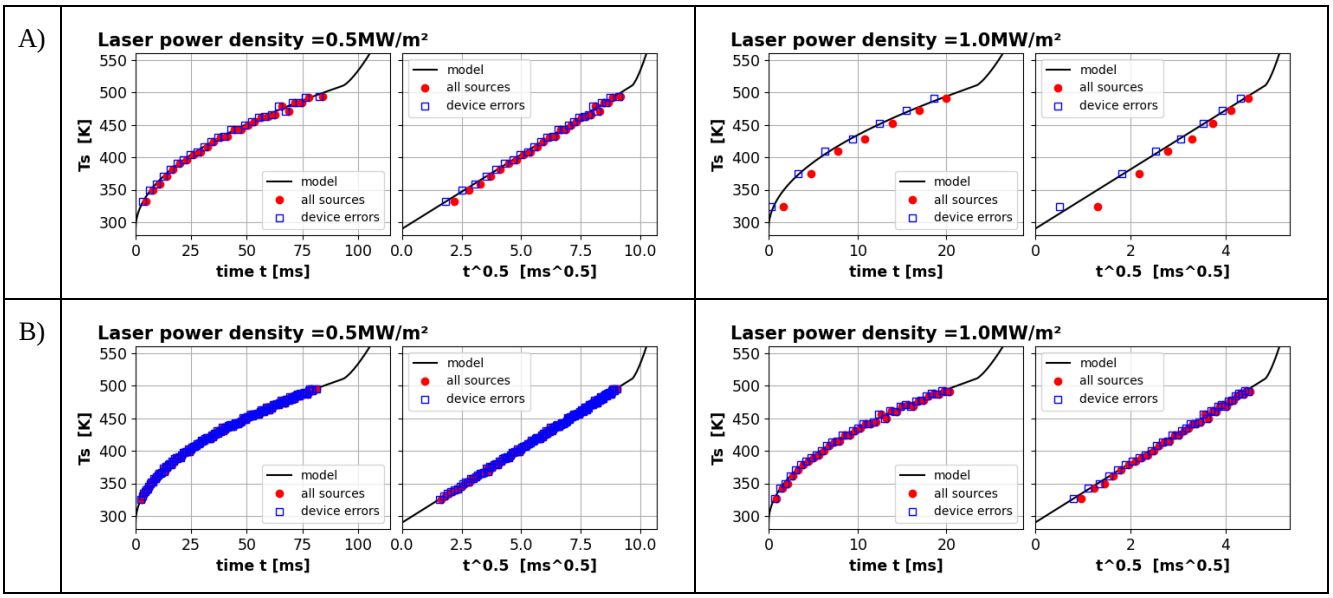

Figure 11. Example of random draws for laser power density 0.5 and 1.0 MW/m².
A) FLIR 300 µs, 328 Hz. B) NOXANT 1700 Hz.

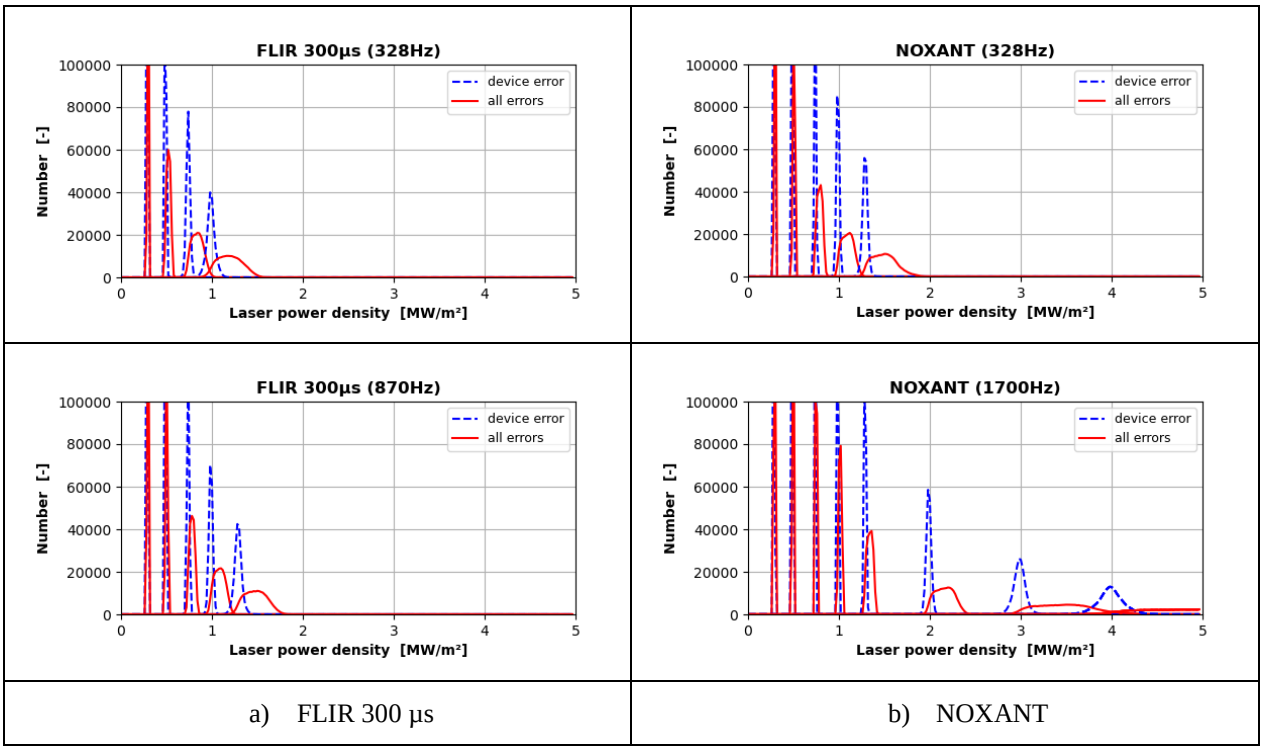

Figure 12. Histograms of estimated laser power density for the two cameras. Two sets of error sources are considered. Blue dash: the two camera error sources. Red line: all three error sources.

DOI: 10.13009/EUCASS2022-4446

a) FLIR 300 µs

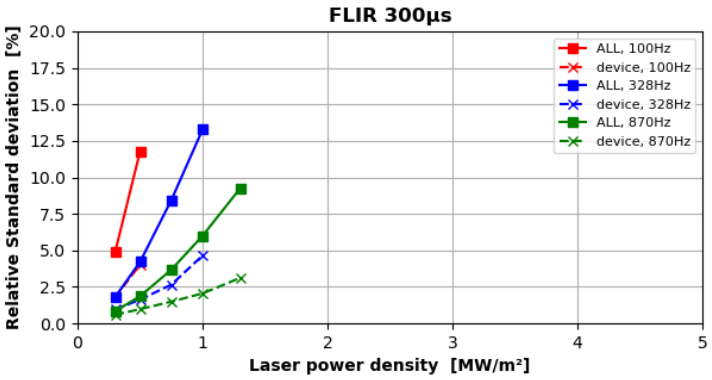

b) NOXANT

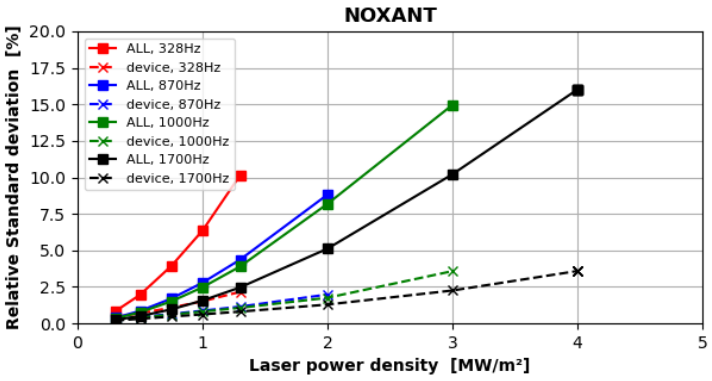

Figure 13. Standard deviations of estimated laser power density for the two cameras at various frequencies, normalized by the power density value.

3.4. Spatial-integration uncertainty induced by Gaussian beam profiles

Here, the focus is placed on the spatial-integration uncertainty associated with the field-of-view integration performed by a measurement device, for instance the radiometer that was used in our experiments.

3.4.1.Laser-beam power density maps for the considered conditions

The three spatial-integration conditions described in sections 2.4.3 are introduced via the associated laser-beam power density maps for a peak power of 0.42 MW/m² (Figure 14). The spatial distributions show the level of laser inhomogeneity for various spatial areas: for the full propellant sample (a) or for a 3 mm-diameter disk equivalent to the radiometer field-of-view (b and c). In the case of the 3 mm-diameter disk, two laser positions relative to the disk are shown: with a center beam (b) or a beam that is laterally shifted by 1.5-mm. The associated power distributions are plotted in Figure 15. The distributions show that the full sample is heated up by local power values ranging from 0.22 to 0.42 MW/m². The interval is much narrower for the radiometer with a centered beam (0.38 to 0.42 MW/m²), which would be the ideal usage of the device. It is observed that a simple 1.5 mm lateral shift spreads the power distribution to the interval [0.29 MW/m²; 0.42 MW/m²].

DOI: 10.13009/EUCASS2022-4446

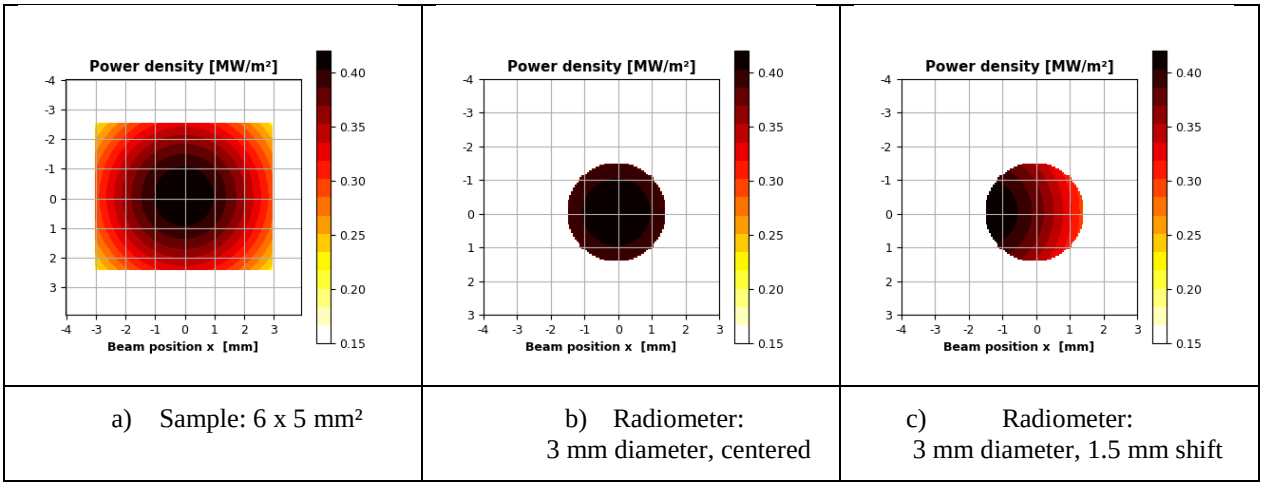

a) Sample: 6 x 5 mm²

b) Radiometer: 3 mm diameter, centered

c) Radiometer: 3 mm diameter, 1.5 mm shift

Figure 14. Laser power density maps for various sample sizes for a peak power of 0.42 MW/m².

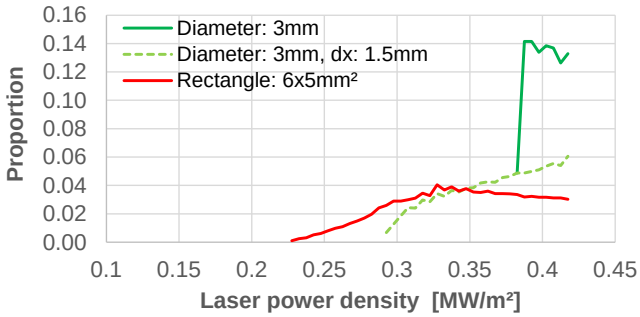

Figure 15. Laser power density distribution for the three areas shown in Figure 14.

3.4.2. Effect of laser-beam profile for an ideal rectangular sample

Surface temperature evolutions are simulated for each local spot of the sample with the assumption that the laser beam is their only heat source. Neglecting the interaction with neighboring parts of the sample is a strong and unrealistic assumptions as soon as some parts of the sample ignite but we believe it to be realistic enough during the inert-heating phase. Still, this assumption leads to interesting trends close to the ignition of the first sample spot.

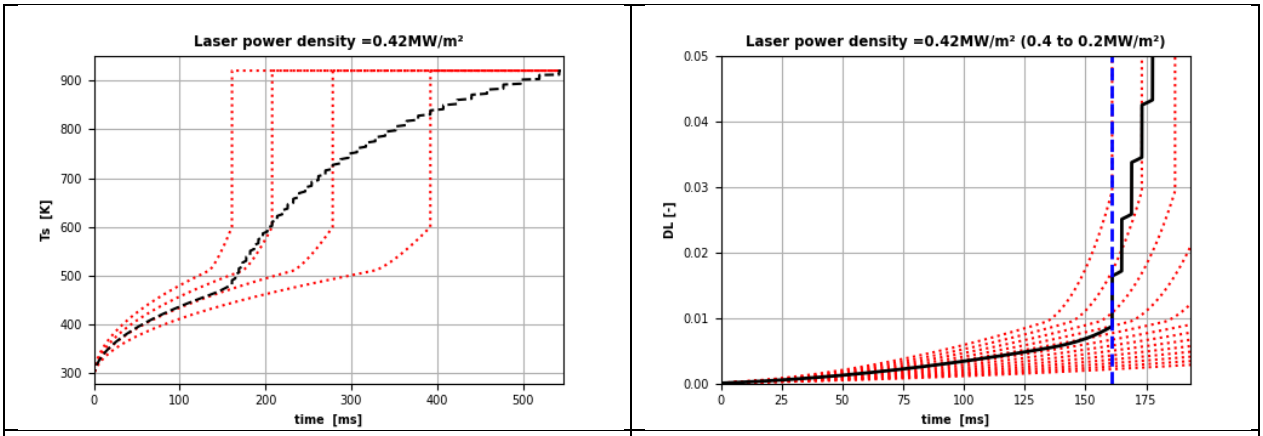

a) Surface temperature

b) Simulated radiometer signal

Figure 16. Surface temperature averaged over a rectangular solid-propellant sample (6 x 5 mm²). Peak power density: 0.42 MW/m².
Red lines: elementary values for local spots. Black line: values averaged over the sample.

DOI: 10.13009/EUCASS2022-4446

Figure 16 shows simulated surface temperature evolutions obtained at various spots of the 6 x 5 mm² sample. The peak laser power density is set at 0.42 MW/m². Examples of local surface temperature are plotted in red whereas the average surface temperature is shown in black. As expected, the average surface temperature is much lower than that of the first ignition spot. Still, the average plot shows a steep slope change at a time corresponding exactly at the moment of the first ignition. For the associated simulated radiometer signal, the slope changes at the moment of the first ignition spot is even steeper (Figure 16 b). It tends to confirm that this device is more sensitive to the first apparition of ignited surface on the sample.
Figure 17 shows two simulated signals for the radiometer, i.e., integrated over the 3-mm diameter collection disk with a centered or a shifted laser beam. A mere 1-5 mm shift leads to a strong signal reduction by a factor of two. However, the slope change happens at the same time since both field-of-views intercept the laser peak power location. A direct analysis of the two signals would then lead to the same ignition delay but to very different estimated power density from the slope. It shows the importance of carefully aligning the laser beam with the radiometer field-of-view, or at least of characterizing the alignment.

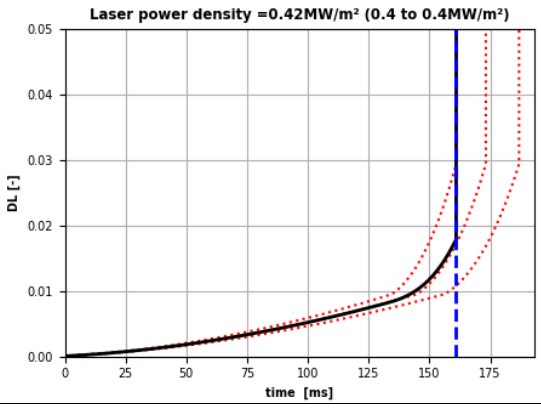

a) 3-mm diameter, centered laser beam

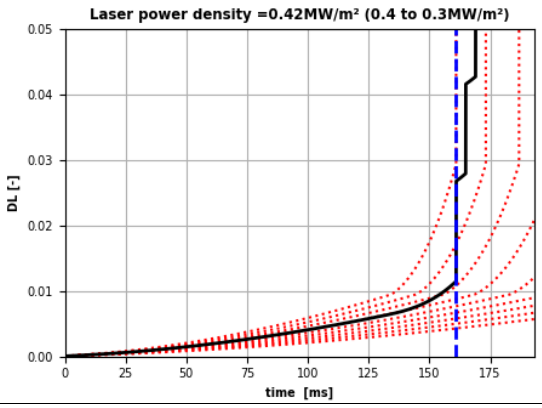

b) 3-mm diameter, 1.5-mm shifted laser beam

Figure 17. Radiometer signal simulated for two laser beam positions relative to the field of view. Red lines: elementary signal for local spots. Black line: Signal averaged over the field of view.

3.4.3. Comparison with a real radiometer data set

The simulated data suggest that luminance averaging over the propellant sample can explain the trends observed for the experimental radiometer data, i.e., a smooth initial slope followed by a steep slope variation at the apparition of the first ignition spot. This is confirmed in Figure 18 a), which compares the radiometer signal to that of the IR camera averaged over the sample,. The corresponding surface temperatures are compared in Figure 18 b). As for the radiometer, the plotted signal refers to that directly measured by the device. As for the IR camera, the relevant quantity for the comparison ("camera – sample") is obtained by averaging the luminance signal over the sample surface and by converting it to a temperature quantity. The temperature evolution of the 1st ignition spot is also included ("camera – 1st spot"). In addition, three sample-averaged simulations are displayed. They correspond to the signal integration conditions defined in section 3.4.1. As expected, the computed temperatures are lower than that of the first ignition-spot. However, the simulated temperatures are still larger than that recorded by the radiometer and that obtained by means of sample-averaging of the IR camera recording.
As for the IR camera, the discrepancy can be explained by the use of an inaccurate laser beam profile in the simulations. Besides, the Gaussian profile of the laser beam used in the experiments is unlikely to be perfectly centered over the sample. Moreover, the Gaussian shape assumption still needs confirmation. This could be achieved by means of a beam profiler. As for the radiometer, the discrepancy is much larger and can be explained by alignment issues. The radiometer may be targeting the edge of the laser beam without intercepting its peak. This would explain the lower slope observed. As such, the apparition of the ignition spot on the sample surface would actually not be detected but the ignition event (steep variation of the slope) would be so, as a result of a vertical flame intercepting the radiometer collection volume The ignition would then appear with an apparent delay. In future works, the radiometer alignment would have to be improved in order to provide estimations of the laser power-density and of the ignition time.

DOI: 10.13009/EUCASS2022-4446

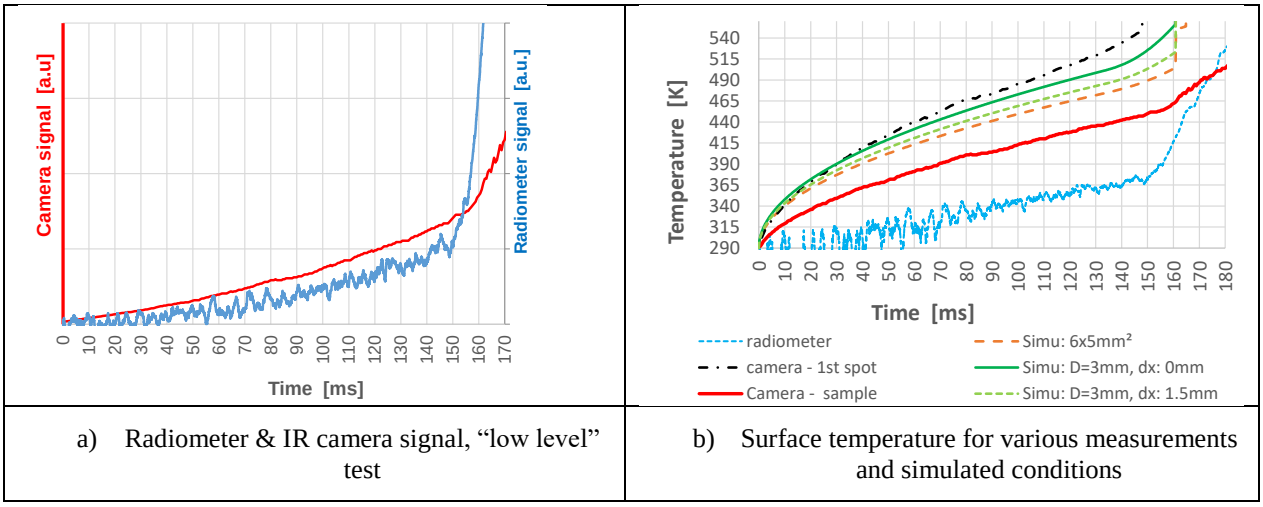

a) Radiometer & IR camera signal, "low level" test

b) Surface temperature for various measurements and simulated conditions

Figure 18. Signal and surface temperature for the "low level" ignition test.

Careful analysis of the data is required in order to estimate laser power density from surface temperature evolution $T_s(t)$. Figure 19 shows the spread of the laser power density estimated for the various temperature plots shown in Figure 18 b). Ignition happens as local hot spots, so the real power density that induces ignitions is the local power density for the first spot, i.e. 0.46 MW/m². But if the IR signal is integrated over the full propellant sample ("camera sample"), the apparent temperature slope leads to a value closer to 0.30 MW/m², showing a risk of power density underestimation when local data is not accessible. It is consistent with the power density obtained from radiometer data. The three simulated spots do show that reduction from the real local value (0.46 MW/m²) down to 0.40 to 0.35 MW/m². The simulated values remains larger than those obtained with the two experimental spatially-integrated conditions (camera sample & radiometer) but this is certainly due to the use of an assumed Gaussian beam profile that might not be consistent with the real profile of the experiments. Characterizing our laser beam will lead to more accurate simulations.

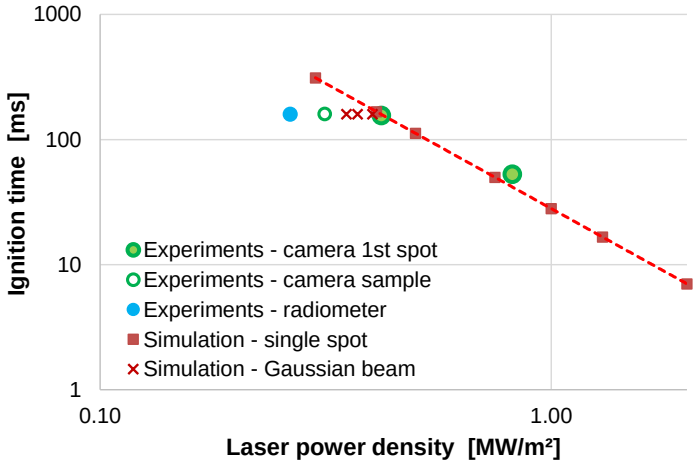

Figure 19. Ignition delay vs laser power density. It includes estimated laser power density for various experimental data and simulations for an ignition delay around 150 µm.

4. Conclusion

A general approach was presented for the purpose of estimating the surface temperature and laser power density of solid-propellant ignition studies. The approach includes a detailed error estimation based on random Monte Carlo draws. The method is based on a simple phenomenological ignition model that was adjusted to ignition experiments and was demonstrated on a research AP/HTPB composition ignited by a laser set at two power levels. The uncertainty study only considered three error sources, focusing on the camera parameters and synchronization aspects. It showed

DOI: 10.13009/EUCASS2022-4446

the larger influence of the camera acquisition rates and trigger synchronization of the laser on the estimation of the laser power density, especially for laser flux larger than 1.0 MW/m². The uncertainty associated to the spatial integration of an inhomogeneous laser beam profile was also revealed by considering a typical Gaussian laser beam profile. Spatially integrated signal shows apparent ignition occurring at the same time as that of the first local ignition spots but with shallower temperature slopes. This induces possible underestimation bias in the evaluation of the incident laser-power density. The approach is very promising for the general purpose of improving the experimental methodology for the determination of surface temperature before ignition and reduce associated error levels. It will also enable providing realistic error bars for the estimated parameters used to adjust ignition models. In futures works, the method will evolve to be more exhaustive by considering additional error sources such as the uncertainties on the surface emissivity or on the thermophysical properties of the solid-propellant sample.

5. Acknowledgment

We want to acknowledge DGA for the funding of the present research work.

6. References

[1] Price, E. W., Bradley Jr, H. H., Dehority, G. L., & Ibiricu, M. M. (1966). Theory of ignition of solid propellants. AIAA Journal, 4(7), 1153-1181.
[2] Linan, A., & Williams, F. A. (1971). Theory of ignition of a reactive solid by constant energy flux. Combustion Science and Technology, 3(2), 91-98.
[3] Linan, A., & Williams, F. A. (1972). Radiant ignition of a reactive solid with in-depth absorption. Combustion and Flame, 18(1), 85-97.
[4] Lengellé, G., Bizot, A., Duterque, J., & Amiot, J. C. (1991). Allumage des propergols solides. La Recherche Aérospatiale, (2), 1-20.
[5] Beckstead, M. W., Puduppakkam, K., Thakre, P., & Yang, V. (2007). Modeling of combustion and ignition of solid-propellant ingredients. Progress in Energy and combustion Science, 33(6), 497-551.
[6] Gallier, S., Ferrand, A., & Plaud, M. (2016). Three-dimensional simulations of ignition of composite solid propellants. Combustion and Flame, 173, 2-15.
[7] Francois, L., Dupays, J., & Massot, M. (2021). A new simulation strategy for solid rocket motor ignition: coupling a CFD code with a one-dimensional boundary flame model, verification against a fully resolved approach. In AIAA Propulsion and Energy 2021 Forum (p. 3695).
[8] Orlandi, O., Fourmeaux, F., & Dupays, J. (2019). Ignition Study at Small-Scale Solid Rocket Motor. EUCASS 2019.
[9] Cain, J., & Brewster, M. Q. (2006). Radiative Ignition of Fine-Ammonium Perchlorate Composite Propellants. Propellants, Explosives, Pyrotechnics: An International Journal Dealing with Scientific and Technological Aspects of Energetic Materials, 31(4), 278-284.
[10] Baer, A. D., & Ryan, N. W. (1965). Ignition of composite propellants by low radiant fluxes. AIAA journal, 3(5), 884-889.
[11] Inami, S. H., McCulley, L., & Wise, H. (1969). Ignition response of solid propellants to radiation and conduction. Combustion and Flame, 13(5), 531-536.
[12] Zanotti, C., & Giuliani, P. (1998). Composite propellant ignition and extinction by CO2 laser at subatmospheric pressure. Propellants, Explosives, Pyrotechnics, 23(5), 254-259.
[13] Atwood, A. I., Ford, K. P., Bui, D. T., Curran, P. O., & Lyle, T. (2009). Radiant ignition studies of ammonium perchlorate based propellants. Progress in propulsion physics, 1, 121-140.
[14] Granier, J. J., Mullen, T., & Pantoya, M. L. (2003). Nonuniform laser ignition in energetic materials. Combustion Science and technology, 175(11), 1929-1951.
[15] Boulal, S., Devillers, R. W., Lestrade, J. Y., Lamet, J. M., Corato, C., Henry, D., & Dupays, J. (2021). Experimental investigation on the heat fluxes generated by AP/HTPB solid propellant flames. *Combustion and Flame*, *228*, 89-98.
[16] Crosland, B. M., Johnson, M. R., & Thomson, K. A. (2011). Analysis of uncertainties in instantaneous soot volume fraction measurements using two-dimensional, auto-compensating, laser-induced incandescence (2D-AC-LII). Applied Physics B, 102(1), 173-183.
[17] Johnson, M. R., Devillers, R. W., & Thomson, K. A. (2013). A generalized Sky-LOSA method to quantify soot/black carbon emission rates in atmospheric plumes of gas flares. Aerosol Science and Technology, 47(9), 1017-1029.